ORIGINAL RESEARCH ARTICLE

Numerical Investigation of Burden Distribution in Hydrogen Blast Furnace

JING LI, SHIBO KUANG, RUIPING ZOU, and AIBING YU

Hydrogen injection is a promising technology currently under development to reduce CO_2 emissions in ironmaking blast furnaces (BFs). Therefore, hydrogen BF is studied by a recent process model based on computational fluid dynamics (CFD). It focuses on the effect of peripheral opening extent (POE), which represents the coke amount near the furnace wall. The simulations consider a 380 m^3 BF operated with hydrogen injection through both shaft and hearth tuyeres. The overall performance of the BF is analyzed in terms of the inner states. It shows that increasing POE hinders the pre-reduction and pre-heating roles of shaft-injected hydrogen (SIH) but improves the CO indirect reduction rate. An optimum peripheral opening extent can be identified to achieve a maximum hot metal (HM) temperature, relatively low bed pressure, and good gas utilization. The interaction between SIH flow rate and burden distribution is also quantified. It shows that the increase in SIH flow rate slows down the CO indirect reduction rate but enhances the H_2 indirect reduction rate. These opposite trends account for the less variation of HM temperature with POE as the SIH flow rate increases. This variation becomes trivial at relatively large SIH flow rates and small POEs. Overall, the POE affects the cohesive zones more than the SIH flow rate. However, under the conditions considered, both variables cannot significantly improve the penetration of the shaft injection, the effect of which is generally confined within the peripheral region.

https://doi.org/10.1007/s11663-022-02672-6

I. INTRODUCTION

THE blast furnace (BF) ironmaking process can efficiently reduce iron from iron ore; however, it relies heavily on fossil fuels like coke and pulverized coal. This process represents about 70 pct of CO_2 emission and energy consumption in an integrated steelworks.[1] Hydrogen injection into blast furnaces is a promising technology to solve this problem. It is currently a hotspot of BF research, as reflected by a few recent reviews on hydrogen blast furnaces (HBFs).[2–7] In the HBF process, hydrogen is used to replace carbon as much as possible for iron ore reduction. This may be realized by injecting hydrogen-bearing materials through hearth tuyeres, shaft tuyeres, or both. Hydrogen as a reductant has various advantages over carbon, such as lower CO_2 emission, better thermal conductivity, lower viscosity and density leading to lower pressure loss, and larger diffusivity favoring iron ore reduction. However, coke is indispensable in the BF ironmaking process to maintain good bed permeability, leading to certain carbon consumption. Also, hydrogen inevitably competes with carbon for iron ore reduction.[8] As such, there exists a limit for hydrogen usage in an HBF. Predicting the hydrogen usage limit and then identifying possible measures to lift this limit represents an important area of HBF research and development.[9]

The burden distribution represents the spatial locations of particles inside a BF, determining the distribution of the gas when flowing through burden materials. Therefore, the gas flow, the associated heat and mass transfer, momentum transfer and chemical reactions, and the cohesive zone (CZ) that largely determines BF overall performance can be significantly affected by burden distribution patterns.[10] As such, burden distribution may affect HBF performance to various extents. In a modern BF, burden materials, including coke and iron ore, are often charged into a BF, generating alternative coke and ore layers. Compared with coke, iron ore has greater resistance to the gas flow due to its smaller size and higher density.[11] Therefore, adjusting

JING LI, SHIBO KUANG, and RUIPING ZOU are with the ARC Research Hub for Computational Particle Technology, Department of Chemical Engineering, Monash University, Clayton, VIC 3800, Australia. Contact e-mail: shibo.kuang@monash.edu AIBING YU is with the ARC Research Hub for Computational Particle Technology, Department of Chemical Engineering, Monash University and also with the Centre for Simulation and Modelling of Particulate Systems, Southeast University - Monash University Joint Research Institute, Suzhou 215123, P.R. China.

Manuscript submitted August 16, 2022; accepted October 7, 2022.
Article published online October 20, 2022.

the burden distribution pattern is a routine operation to change the gas distribution to achieve expected BF performance. Changing the radial profile of the ore-to-coke ratio (O/C) is one of the most important aspects of burden distribution control, which becomes complicated for HBF. In particular, the hydrogen injected into a HBF through hearth and tuyeres interact with each other and with other gas components like CO and nitrogen. Burden distribution control must consider these interactions to achieve the optimum HBF performance and maximize the hydrogen usage. However, so far, it is unclear how various gas components interact with each other and affect HBF performance under different radial O/C profiles. Therefore, it is necessary to overcome this problem toward the successful industrialization of HBF.

In the past, extensive efforts have been made to study the effects of burden distributions. For instance, various measuring techniques such as probes,[12,13] radar,[14] or metal grids measurement[15] were developed to study burden trajectory, filling points, and burden profiles. Scaled-down burden charging systems were also established to understand burden formation in the BF throat.[16] Although useful, it is still challenging to experimentally quantify the effect of burden distribution on BF performance directly. Therefore, the development and application of numerical models predicting the effect of burden distribution have attracted much interest.[11,17,18] Most numerical models used to study burden distributions were based on the discrete element model (DEM), focusing on conventional BF operations.[19–21] To our knowledge, very few efforts were made to use the combined approach of DEM and CFD (computational fluid dynamics) to study the effect of burden distribution on the shaft injection.[22] Nevertheless, the previous DEM/CFD-DEM studies of burden distributions mainly considered the operations under room temperatures and thus ignored the associated thermochemical behaviors. To date, even for conventional operations, the effect of burden distribution on BF performance has not been fully studied using DEM-based models. This is mainly because such an approach has prohibitively high computational requirements when simulating industrial BFs.

On the other hand, the CFD process models have been widely adopted to simulate BFs to obtain the inner states and global performance under industrial operating and geometric conditions. This situation benefits from the continuous contributions of many investigators, as summarized elsewhere.[23–25] Using CFD BF process models, conventional and new BF processes have been extensively studied under different conditions.[24] In recent years, they were also used to study HBFs. For instance, a CFD BF process model is adopted by Nogami *et al.*[26] to study the BF operated with varying hydrogen enrichment through hearth tuyeres from 0 to 43.7 pct. *Via* the same model, Tang *et al.*[27] revealed the influence of hydrogen injection with the hydrogen enrichment of up to 15.23 pct; Chu *et al.*[28] compared the hydrogen-bearing material injection with all-coke operations. Li *et al.*[29] evaluated the effects of the belly injection of reformed coke oven gas (RCOG), hot burden charging, and their combination on BF performance using a 2D process model. Using a similar model, Yu and Shen[18] studied how the shaft injection of pure hydrogen affected BF performance. Recently, the current authors extended their three-dimensional (3D) CFD BF process model to simulate an HBF, where the hydrogen enrichment through hearth tuyeres changes from 3 to 49.5 pct.[8] The model predicted a minimum coke rate corresponding to a hydrogen usage limit. All the previous studies of HBF have improved our understanding of this new technology. So far, the efforts dedicated to studying the effect of burden distribution inside an HBF are lacking. However, burden distribution somewhat affects the penetration depth of shaft-injected hydrogen into the bed column of an HBF, changing the interaction between H_2 and CO and the utilization efficiency and ultimate usage of hydrogen in the furnace. Currently, the knowledge in this respect is very limited. However, it is highly expected to explore the innovative HBF ironmaking technologies.

In this paper, the effect of top burden distribution is studied based on an industrial BF using a validated 3D CFD process model recently reported for HBF.[8] The BF is operated with hydrogen injection through both shaft and hearth tuyeres. Various top burden distribution patterns are particularly considered in terms of peripheral opening extent (POE). The POE represents the coke amount near the furnace wall. Moreover, this study also considers the interaction between the POE and the flow rate of shaft-injected hydrogen. The inner states of the BF are analyzed and linked with the overall performance. This study clarifies the roles of the peripheral opening operation in affecting hydrogen utilization and usage in a BF.

II. MODEL DESCRIPTION

A validated 3D steady-state multi-fluid model simulating HBF has been adopted in this work. For brevity, only the main model features are outlined. However, various model details can be found elsewhere.[8,30–32] This model simulates the region between the slag and burden surfaces, considering the gas, solid, and liquid phases. The liquid phase consists of molten slag and iron. Each phase is assumed to be a continuous fluid, having one or more components.[8,30–32] Figure 1 shows the model framework, which is, in principle, similar to other BF process models developed by different research groups.[33,34] However, the current BF model integrates a range of sub-models simulating important local phenomena, as detailed elsewhere.[11,17,30,31,35–37] These include the layered structure of burden and CZ, deadman, gas and liquid re-distribution by layered CZ and raceway, trickling liquid flow in the dripping zone, and productivity related to stockline variation. Based on the carbon balance, the model automatically adjusts the burden charge rate to simulate the stockline variation. As a result, the productivity adapting to certain in-furnace states under given BF conditions can be predicted (see Figure 1), as detailed previously.[11,17,38] Therefore,

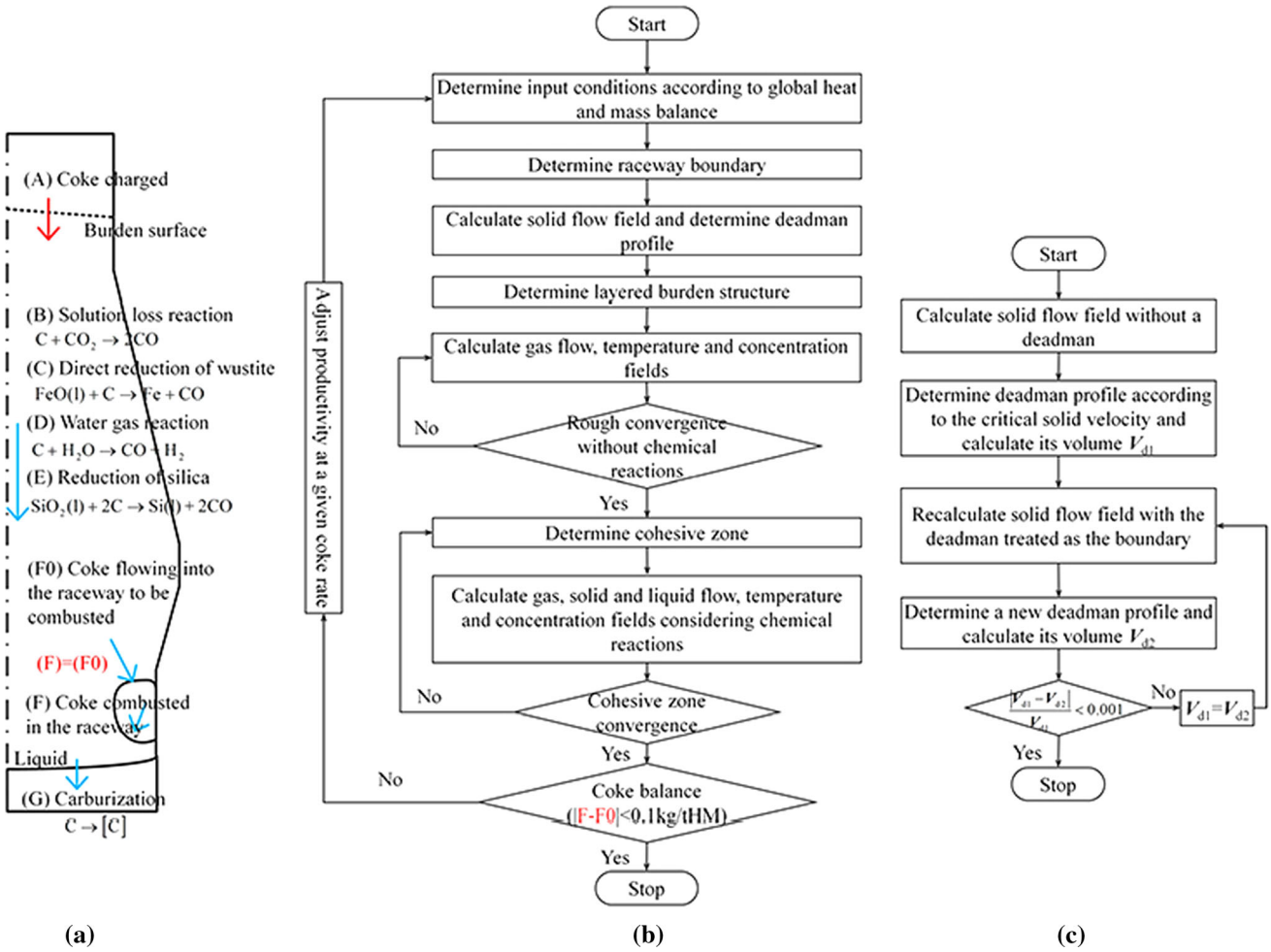

Fig. 1—Framework of the present CFD BF process model: (*a*) coke balance modeling, (*b*) solution procedure, and (*c*) sub-model for determining deadman profile.

the productivity is a simulation output that varies with BF conditions. The validation of the model has considered a range of applications, confirming the applicability of the model. The validation results are not included in this paper to avoid repetition.[8,30–32]

III. SIMULATION AND BOUNDARY CONDITIONS

Figure 2(a) presents the geometric and grid representation of the simulated HBF. It has a volume of 380 m^3 and 14 hearth tuyeres, the same as the previous one.[8] The computational domain is one-seventh of the BF, containing two hearth tuyeres and one shaft tuyere. This setup allows for achieving good computational efficiency while maintaining good grid quality. The two axial planes are set as symmetry planes. The burden materials, loaded into the BF at the top, include coke, iron ore, and flux. The batch weight of iron ore in the loading is 11.1 tonnes, and the coke rate is 433 kg/tHM.

Figure 2(b) presents the burden radial profiles of O/C ratios at the burden surface. Generally, burden distributions are categorized into three types: central opening, uniform, and peripheral opening. The term "opening" means a region charged with more coke and thus having better bed permeability. This study adopts a central-opening burden distribution following the common BF practice (see Figure 2(b)).[11,30,39,40] It is combined with various peripheral opening operations, described by different POE values. Correspondingly, the coke amount in the peripheral region within 20 pct of the radius varies, leading to different O/C profiles. The POE value, which equals the angle between an O/C curve and the horizontal line, varies between − 90 and 90 deg. A larger value means more coke loaded in the peripheral region. The POE is negative when the peripheral region has a thicker ore layer than the middle region; otherwise, it is positive. Note that a fixed coke rate is considered in all the simulations. In these circumstances, if more coke or lower O/C values appear near the wall, the ore layer in the remainder of the radial locations becomes thicker. Moreover, the O/C profile in the circumferential direction remains the same in each simulation.

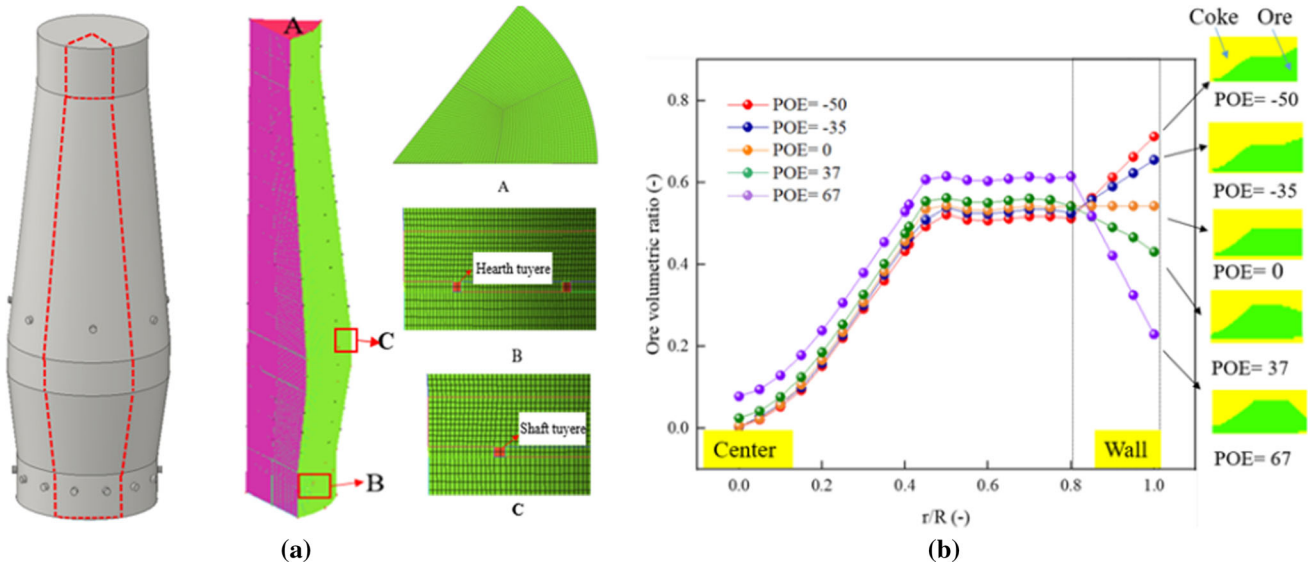

Fig. 2—(*a*) Geometric and grid representation of the simulated HBF and (*b*) corresponding top burden distributions.

The injection of 40 °C pure-H_2 through hearth tuyere is at a flow rate of 6.5 Nm^3/s. This injection rate leads to a minimum coke rate for the current HBF when injecting hydrogen only through hearth tuyeres, as detailed elsewhere.[8] The pulverized coal injection (PCI) rate is fixed (145 kg/tHM). The local heat and mass balance method is used to determine the inlet gas conditions, which are the components, volumetric flow rate, and temperature of the reducing gas in the raceways. The same inlet temperature and flow rate are maintained in all the simulations. The shaft injection of hydrogen is also applied with a pre-heated temperature of 900 °C. The flow rates of shaft-injected hydrogen (SIH) vary between 3 and 6 Nm^3/s.

An in-house Fortran F90 code is adopted to solve the model coupled with the boundaries above, developed based on the open-source code CAFFA3D.[41] Sixty-six CPUs are assigned to each simulation, lasting up to 96 hours. The results are considered to be converged, following standard CFD convergence criteria. Moreover, the solution satisfies the criterion that the CZ profiles in two consecutive iterations differ by less than 0.1 pct, where the CZ profile is quantified using the volume ratio of lumpy and dripping zones.

IV. RESULTS AND DISCUSSION

A. *Effect of POE*

Figure 3 presents the effects of burden distribution in terms of POE (peripheral opening extent) on the overall performance indicators of BF, including HM (hot metal) temperature, productivity and bed pressure, top gas temperature, CO_2 emissions, and utilization factors. The SIH (shaft-injected hydrogen) flow rate is 3 Nm^3/s. As the POE increases from − 50 to 67, the HM temperature first increases gradually to a maximum (when POE = 0) and then drops sharply (Figure 3(a)). Note that the increase in HM temperature essentially represents the potential of coke saving, as detailed elsewhere.[8,38] On the other hand, the productivity in Figure 3(b) decreases first and then increases, opposite to the trend of the HM temperature. The HM temperature and productivity changes will be later explained using inner states. Additionally, a larger POE leads to a reduced pressure drop in the BF (Figure 3(b)) and a lower top gas temperature (Figure 3(c)). Increasing POE improves the bed permeability near the wall. Also, the strong interaction between SIH and iron ore reduces. In these circumstances, the gas pressure drops. In Figure 3(c), CO_2 emissions per tonnage of HM are also included, which become larger at a larger POE. Meanwhile, as the POE increases, the CO and H_2 utilization factors show opposite trends, where the former increases and the latter decreases (Figure 3(d)). This should be because increasing the POE reduces the contact between iron ore and shaft-injected hydrogen. Thus, the H_2 is less utilized, which hinders the competition of H_2 with CO and thus favors CO utilization, generating more CO_2. Overall, an optimum peripheral opening extent (*i.e.*, POE = 0) can be identified according to the highest HM temperature, relatively low bed pressure drop, and good gas utilization. Under this condition, both H_2 utilization efficiency and productivity are reasonably high, as expected. These results suggest that excessive peripheral opening does not significantly improve the shaft injection operation to overcome the problem of shallow penetration. Moreover, because of the relatively low viscosity and density of hydrogen, a uniform burden distribution does not cause a sharp increase in pressure drop. This favorable phenomenon should also benefit from the central opening, whose combination with a uniform burden distribution avoids the pressure build-up in a BF.[11]

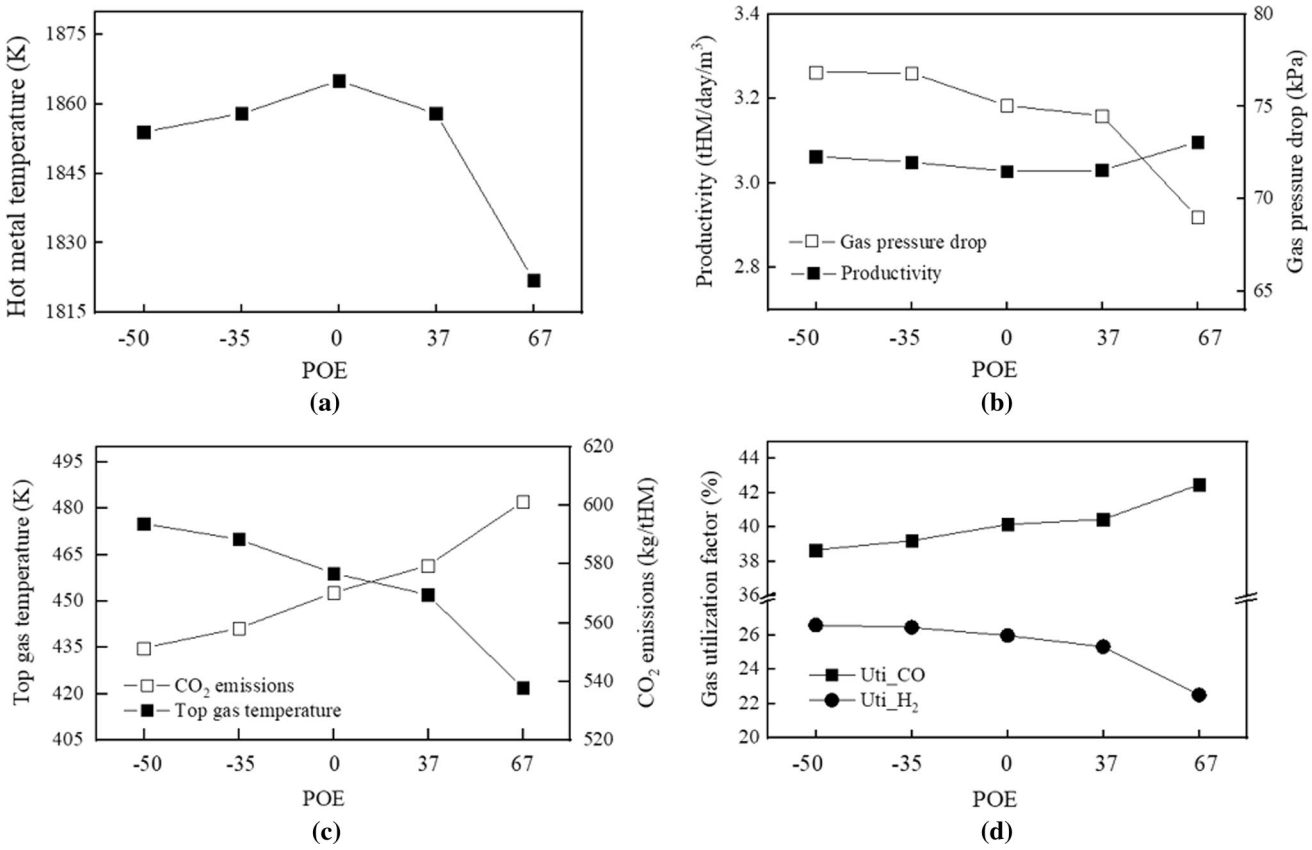

Fig. 3—Overall performance indicators as a function of POE: (*a*) hot metal (HM) temperature, (*b*) productivity and bed pressure drop, (*c*) top gas temperature and CO_2 emissions, and (*d*) gas utilization factors.

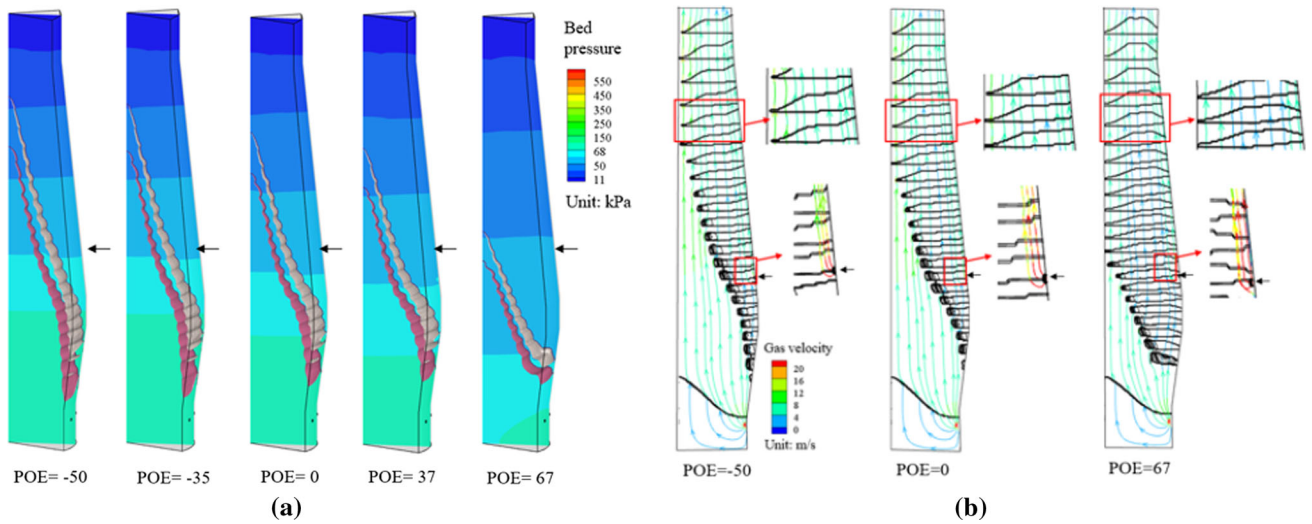

Fig. 4—(*a*) Cohesive zone (CZ) and bed pressure distribution and (*b*) gas flow fields at different POEs.

The inner states governing the overall BF performance are analyzed to understand the overall performance of BF further. Figure 4 compares the CZ profiles, bed pressure distributions, gas flow fields, and ore layers at different POEs. As the POE increases, the CZ head drops significantly, and the root lifts slightly. As a result, a less inclined CZ with a shorter total length is observed (Figure 4(a)). It is established that significant resistance occurs to the gas flow when flowing through the CZ, especially in the melting ore layer that has low permeability. This shortened CZ length helps reduce pressure drop. Essentially, the CZ change with POE is controlled by the development of the gas flow corresponding to various burden distribution patterns in Figure 4(b).

More iron ore near the wall (r/R = 0.8–1.0) with increasing POE is taken out and uniformly redistributed in the remainder of radial locations. Correspondingly, the gas flow is more developed in the peripheral region than in other radial locations. This can be seen clearly from the color of the flow streamlines, representing gas velocity magnitudes. Notably, the gas velocity magnitudes in the middle region in the radial direction reduce significantly at a higher POE because the ore layer with relatively low permeability becomes thicker there. At the same time, the gas velocity magnitudes above the shaft injection level become larger near the wall. However, such a region does not change significantly in the radial direction. In other words, the shafted-injected hydrogen is mainly confined within the peripheral region. The change of POE does not significantly improve the penetration of the shaft-injected hydrogen into the bed column.

Figure 5 demonstrates how the POE affects the temperature contours of gas and solid phases, whose patterns are similar. When the POE becomes larger, the solid/gas temperature drop is observed in the dry zone, corresponding well to the change in top gas temperature in Figure 3(c). Additionally, relatively low temperatures are present above the shaft injection level, which enlarges with the increase of POE. This should be because the thicker ore layer in the middle between the wall and the center reduces the fraction of the gas flow there, as shown in Figure 4(b). Moreover, the heat loss through the wall increases with increasing POE. This is particularly the case near the shaft injection level, where the solid temperature in the peripheral region becomes higher at a larger POE. Moreover, the increased productivity at the largest POE brings more cold burden materials for heating with the same energy input, lowering the temperature in the entire dry zone. As such, it can be concluded that the increase in POE somewhat improves the penetration of SI hydrogen but is still confined in the peripheral region. This improvement does not make the shafted-injected hydrogen more helpful for pre-heating the burden materials near the wall.

Figure 6 demonstrates how the POE affects CO and H_2 indirect reduction rates. Overall, the state of the indirect reduction reaction is in line with BF performance. The H_2 indirect reduction, which is endothermic, mainly happens in the shaft injection region and the lower part of the dry zone. The relatively high temperature and/or good H_2 atmosphere account for these phenomena. In contrast, the CO indirect reduction, slightly exothermic, starts from the region with relatively low furnace temperature, close to the burden surface. With increasing POEs, the CZ moves downwards, enlarging the dry zone and thus improving the overall CO indirect reaction rate. However, the H_2 indirect reduction rate contributing to the pre-reduction generally decreases. The drop near the shaft injection tuyeres should be because of the reduced contact between H_2 and iron ore resulting from the increased velocity magnitudes of shaft-injected hydrogen and the less iron ore near the wall at a larger POE. The decrease in other places is caused by the reduced temperature, as shown in Figure 5.

The indirect reduction rates due to various gas components are quantified (see Figure 7) to look for insights into the indirect reduction reactions, including hearth-generated CO (CO), shafted-injected hydrogen (SIH), and hearth-injected hydrogen (HIH). This is realized by summing the indirect reduction rate stored on each CFD cell for each gas component. For comparison, the result in Figure 7 is expressed as per tonnage of HM. As the POE increases, the total indirect reduction rate increases initially to a maximum and then decreases, showing a similar trend of HM temperature in Figure 3(a). It is established that the direct reduction rate occurring in the CZ and the region below has an opposite trend to the indirect reduction rate. Thus, it decreases to a minimum and then increases. A larger direct reduction rate consumes more coke, which

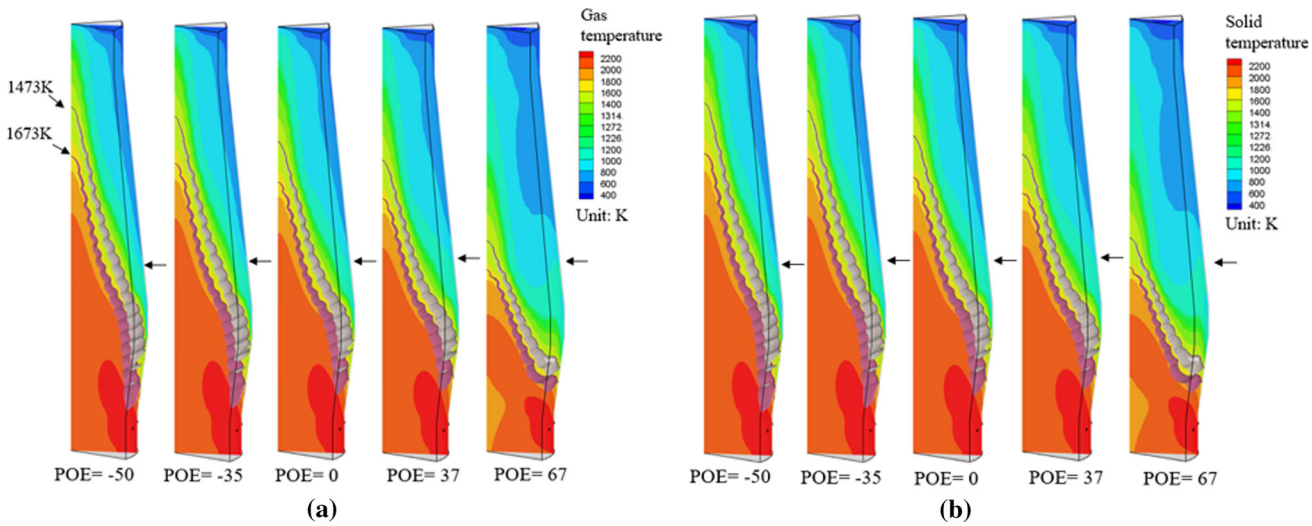

Fig. 5—Effects of POE on (*a*) gas and (*b*) solid temperatures.

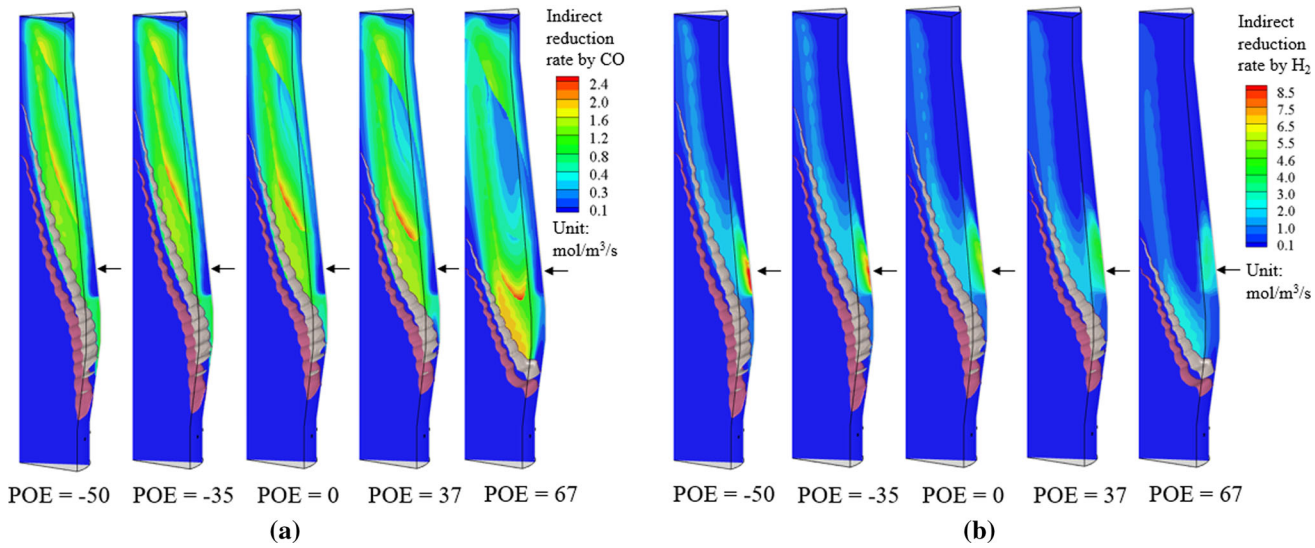

Fig. 6—(*a*) CO and (*b*) H_2 indirect reduction rates at different POEs.

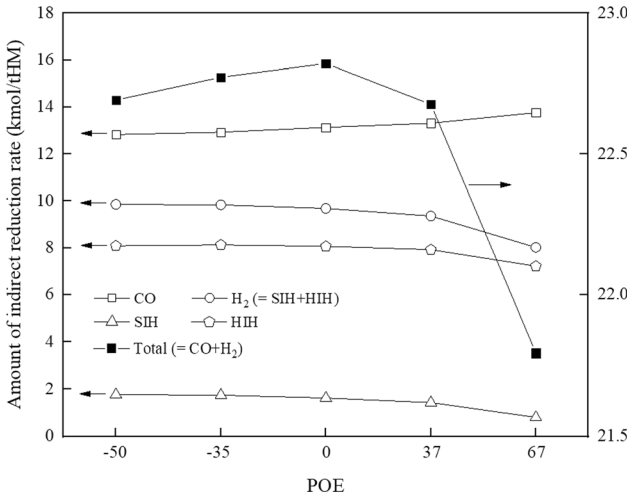

Fig. 7—Indirect reduction rates as a function of POE.

provides more space for the iron ore, increasing productivity. This result explains why the largest POE leads to the lowest indirect reduction rate but gives the highest productivity. Moreover, the significant heat sink caused by the direct reduction decreases the HM temperature. Therefore, the indirect reduction rate and HM temperature have the same trend. Figure 7 also shows that the indirect reduction rates due to HIH and SIH have the same trend as the total indirect reduction rate. This trend is opposite to that of CO indirect reduction rate at relatively large POE values. These results correspond well with the gas utilization efficiency shown in Figure 3(d). In summary, a large POE improves the peripheral gas flow and weakens the central gas flow, lowering the CZ and thus enlarging the dry zone. This situation enhances the CO indirect reduction and hinders the H_2 indirect reduction. In particular, an excessive peripheral opening causes a substantial drop in the total indirect reduction rate and is thus not recommended. As such, optimizing the central-opening extent, as done in our previous studies of conventional BFs,[11,40] should also be considered in future to lift the hydrogen usage limit in an HBF.

Figure 8 demonstrates how the POE affects the mass flow rate and temperature of the liquid phase. Generally, the peripheral liquid flow rate decreases with increasing POE, leading to a more radially uniform liquid flow. This phenomenon is attributed to the less inclined CZ. Note that the central region has a lower gas temperature than the peripheral region (see Figure 5(a)). A more uniform liquid flow distribution enhances the chance of the liquid contacting the high-temperature gas, which can be derived by comparing gas temperature and liquid flow rate distributions. However, the significantly lowered CZ at the largest POE (*e.g.*, 67 here) reduces the distance for the gas to heat the liquid flow, especially in the central region. This factor, together with the increased liquid flow rate resulting from the increased productivity, causes a significant drop in the liquid temperature at the POE of 67. This result highlights the importance of CZ shape and position, which are affected significantly by POE values. Additionally, both Figures 4(b) and 8(a) suggest that a thick fused iron layer forms at the CZ root for the largest POE. This thick layer intensively interacts with the high-speed gas flow, likely causing unsmooth operations.

B. *Interaction Between POE and SIH Flow Rate*

Shaft injection is generally implemented at different flow rates, which may significantly affect its effectiveness.[42] Therefore, the effect of POE is also examined with respect to the SIH flow rate. Here, the flow rate varies between 3 and 6 Nm^3/s. For comparison, other conditions such as coke rate, theoretical flame temperature, and bosh gas flow rate are kept the same. Figure 9 demonstrates how the POE affects the overall performance indicators at different SIH flow rates. With increasing POE, the HM temperature rises to a maximum and decreases dramatically (Figure 9(a)).

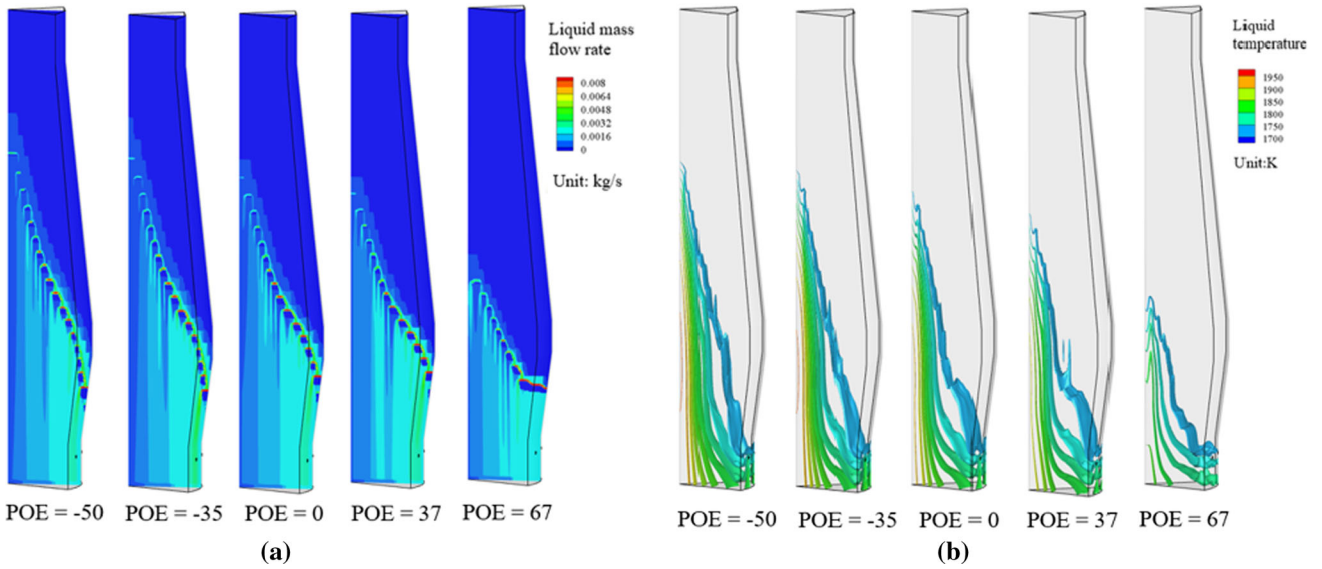

Fig. 8—(*a*) Mass flow rates and (*b*) temperatures of the liquid phase at different POEs.

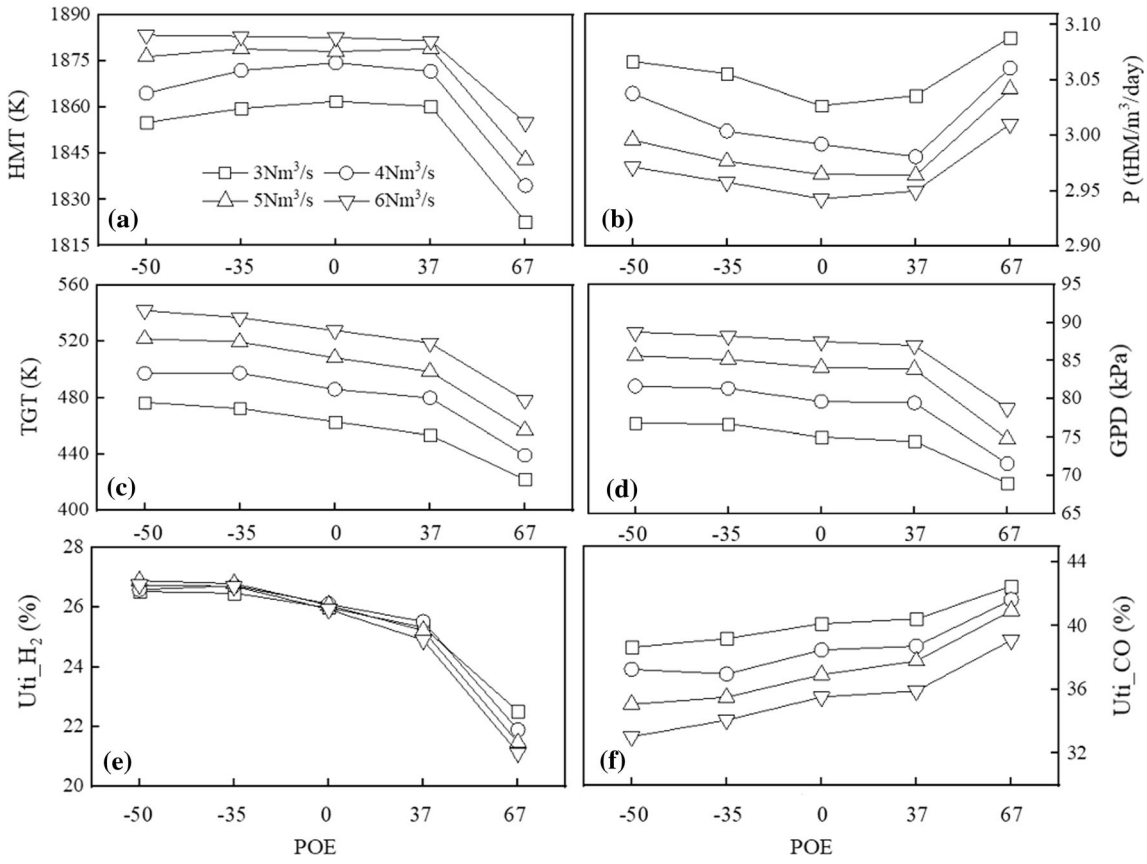

Fig. 9—Effect of POE on BF performance at different SIH flow rates: (*a*) liquid temperature (LT), (*b*) productivity (P), (*c*) top gas temperature (TGT), (*d*) pressure drop (GPD), and gas utilization factors (Uti) of (*e*) H_2 and (*f*) CO.

However, this rise becomes gradual and even not noticeable as the SIH flow rate becomes higher. Moreover, the rise in the HM temperature resulting from the increase in the SIH flow rate other than the POE slows down when the flow rates are relatively high. The productivity trends with POE and SIH flow rate are opposite to that of HM temperature (Figure 9(a)). In contrast, both top gas temperature and pressure drop increase as the SIH flow rate increases (Figures 9(c) and (d)). However, the interaction between the POE and

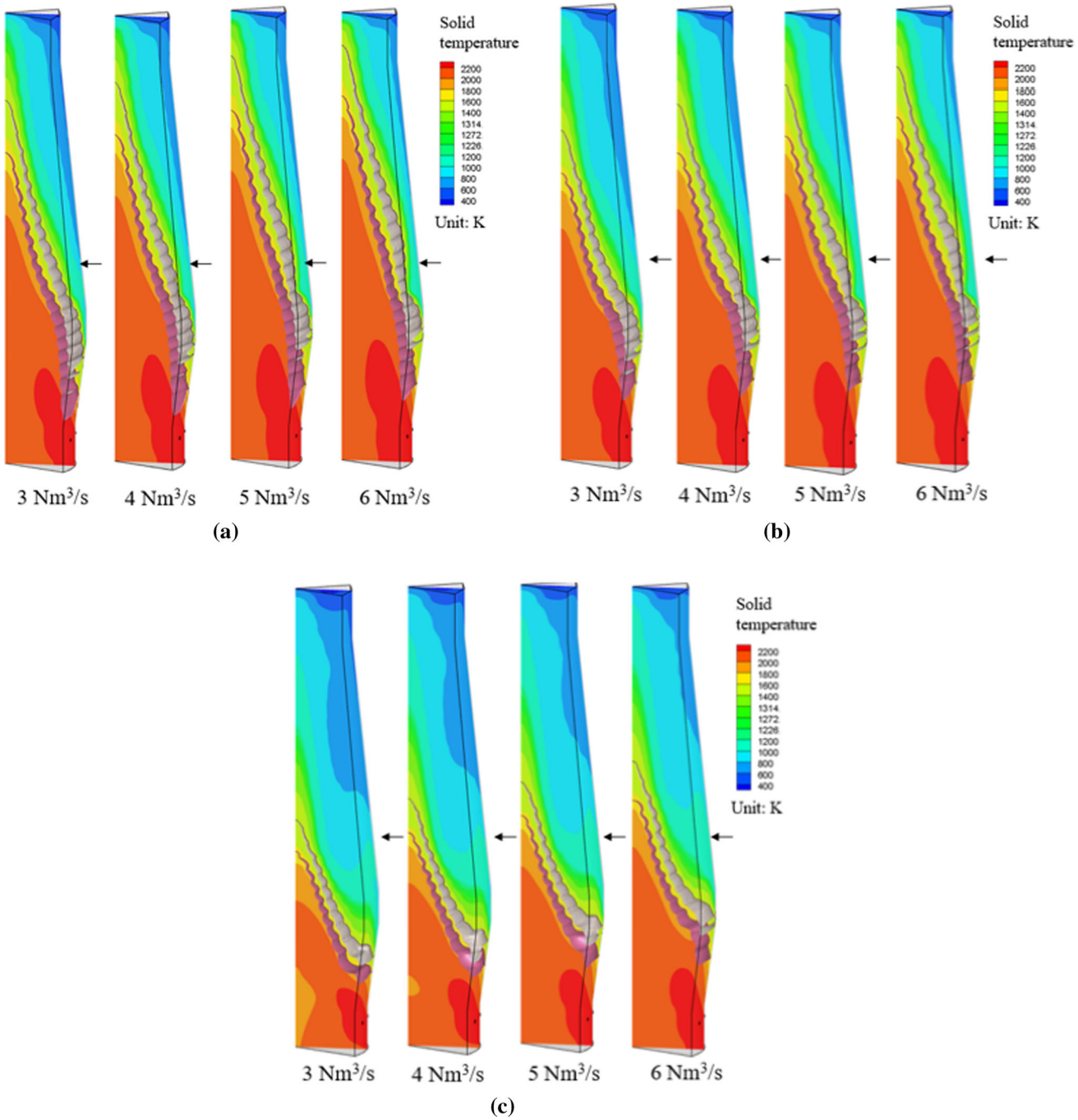

Fig. 10—Solid temperatures at different SIH flow rates for the POE of (*a*) − 50, (*b*) 0, and (*c*) 67.

SIH flow rate differs for various gas components. The curves showing the change of H_2 utilization efficiency with POE are almost the same at different injection rates, especially when the POE is not large (Figure 9(e)). Conversely, the CO utilization efficiency curve shifts down as the injection rate increases (Figure 9(f)). The result suggests that the H_2 utilization efficiency is affected by the POE but not by the SIH flow rate. In the following, the inner states of BF are analyzed to understand the results in Figure 9.

Figure 10 compares the solid temperature distributions with respect to SIH flow rate at three representative burden distributions (*i.e.*, POE = − 50, 0 and 67). The results show that the furnace temperature increases with increasing SIH flow rate for a given POE, lifting the CZ correspondingly, especially the CZ head. Consequently, the CZ becomes more inclined. As expected, a higher shaft injection rate enhances the temperature in the peripheral region of the shaft. This thermal improvement is more apparent at the POE of 67 for relatively

large SIH flow rates (*e.g.*, 5 and 6 Nm^3/s). Such a phenomenon is attributed to more coke loaded near the wall, leading to better bed permeability there. Overall, the POE affects the CZ more significantly than the SIH flow rate under the conditions considered. More specifically, increasing the SIH flow rate does not lift the CZ at the POE of 67 to the positions at the POE of -50 and 0. This result indicates that CZ control is more likely to be achieved through burden distribution modification rather than shaft injection.

Figures 11 and 12 show the contours of CO and H_2 indirect reduction rates with respect to the SIH flow rate for the three burden distributions. Like temperature distributions, the reduction rate distributions are mainly controlled by the burden distribution other than the SIH flow rate. Therefore, the reduction rate profiles are similar at different SIH flow rates for a given POE. However, the spatial distributions of CO/H_2 indirect reduction rate are similar only when POE = − 50 and POE = 0. They are different from those at POE = 67.

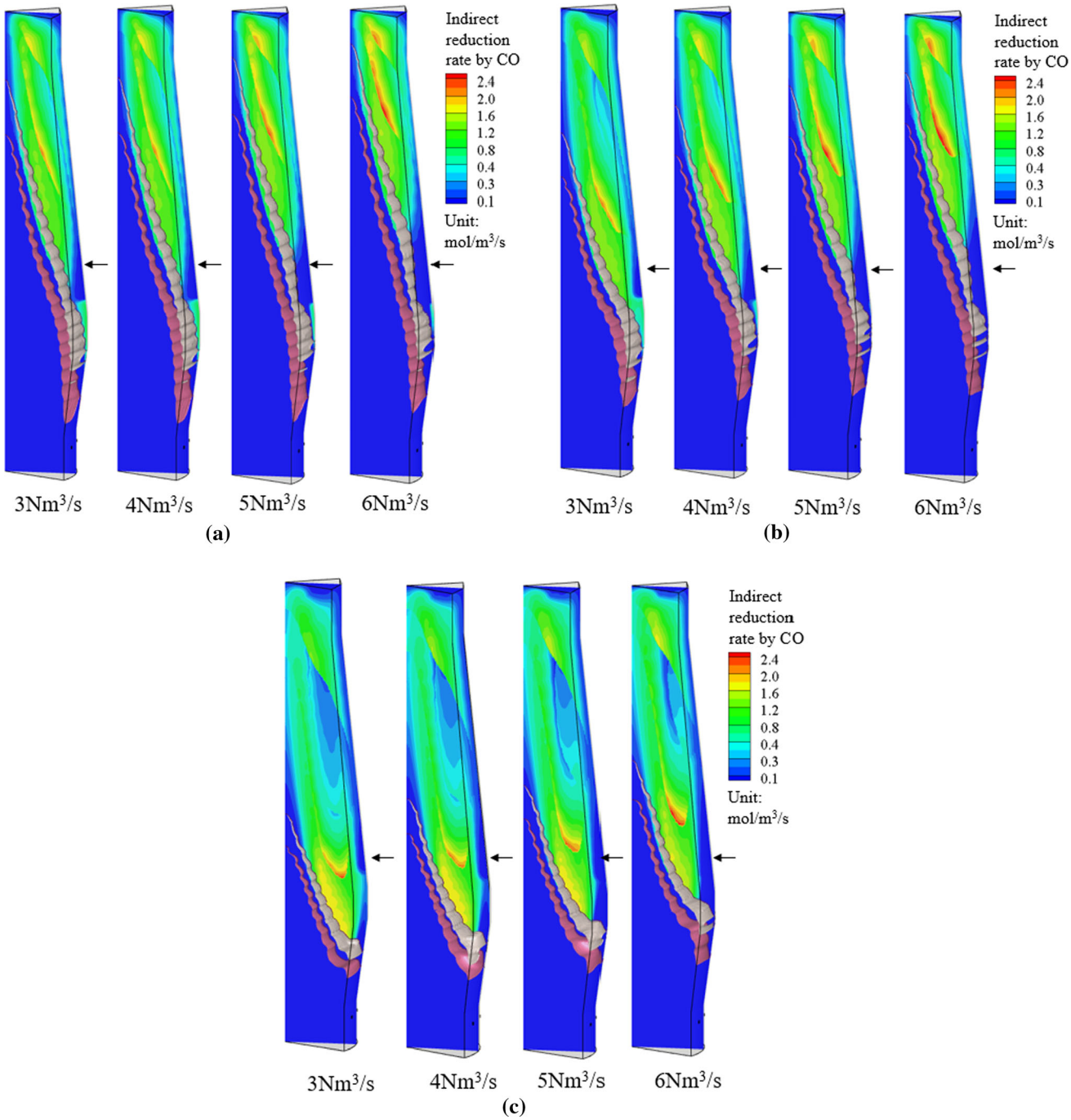

Fig. 11—Indirect reduction rates by CO at different SIH flow rates for the POE of (*a*) − 50, (*b*) 0, and (*c*) 67.

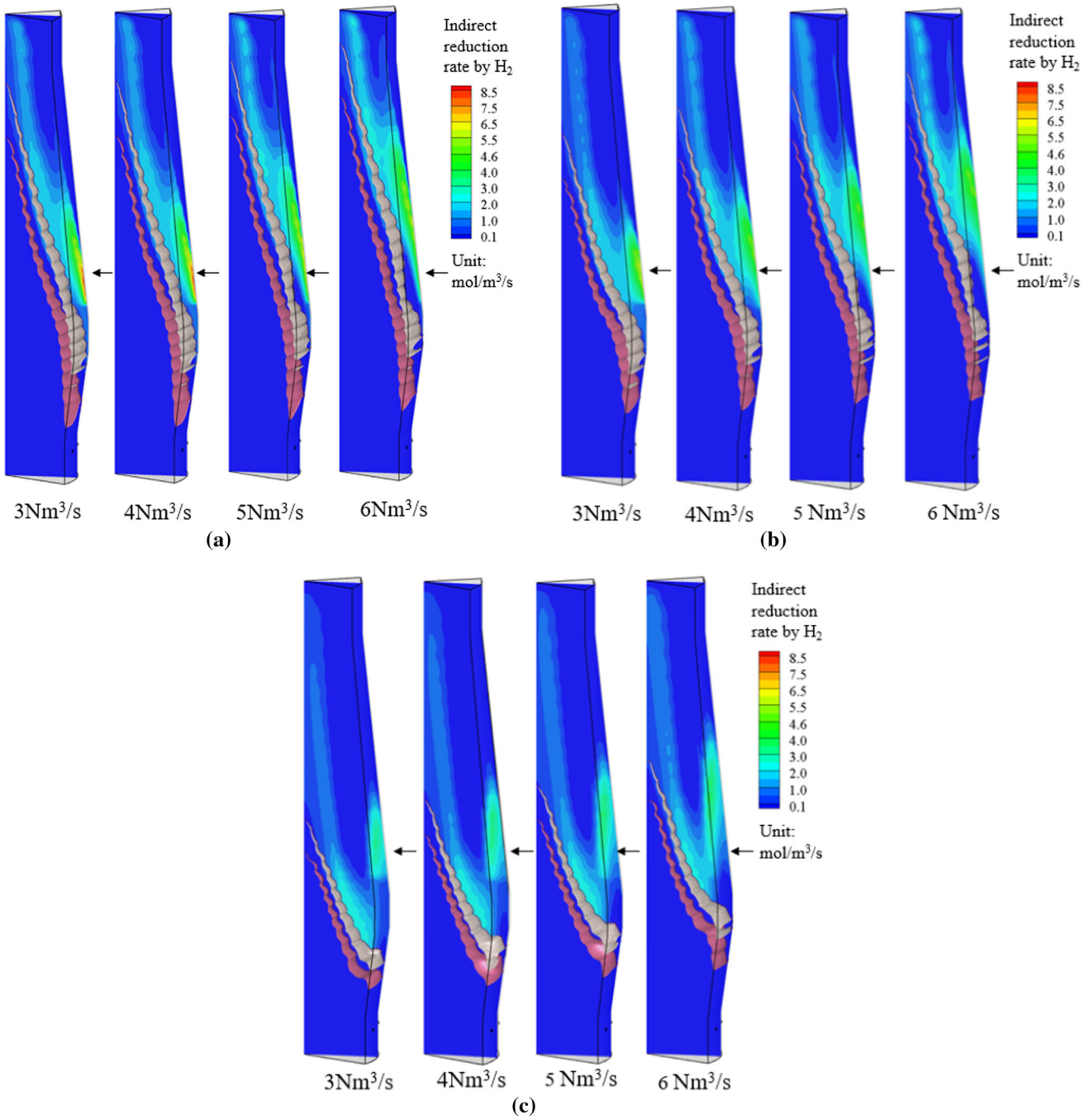

Fig. 12—H_2 indirect reduction rates at different SIH flow rates for the POE of (*a*) − 50, (*b*) 0, and (*c*) 67.

Generally, as the SIH flow rate increases, the peripheral region with observable H_2 indirect reduction rates enlarges (Figure 12), attributed to the temperature elevation by the shaft injection in the upper part of BF. This temperature elevation increases the indirect reduction rate due to CO as well. However, H_2 competes with CO in the peripheral region, and the H_2 indirect reduction plays a dominating role. Because of the enlarged region for the H_2 indirect reduction, the region for the CO indirect reduction is shrunken (Figure 11).

Figure 13 quantitatively compares the indirect reduction rates due to different gas components, including CO, SIH, and HIH, with respect to POE at different SIH flow rates. As discussed, the total indirect reduction rate increases to a maximum and drops drastically as the POE increases while keeping a constant SIH flow rate (Figure 13(a)). However, this non-monotonous phenomenon can only be observed at relatively low SIH flow rates (*e.g.*, 3 and 4 Nm^3/s). Moreover, the total indirect reduction rate with the SIH flow rate is initially

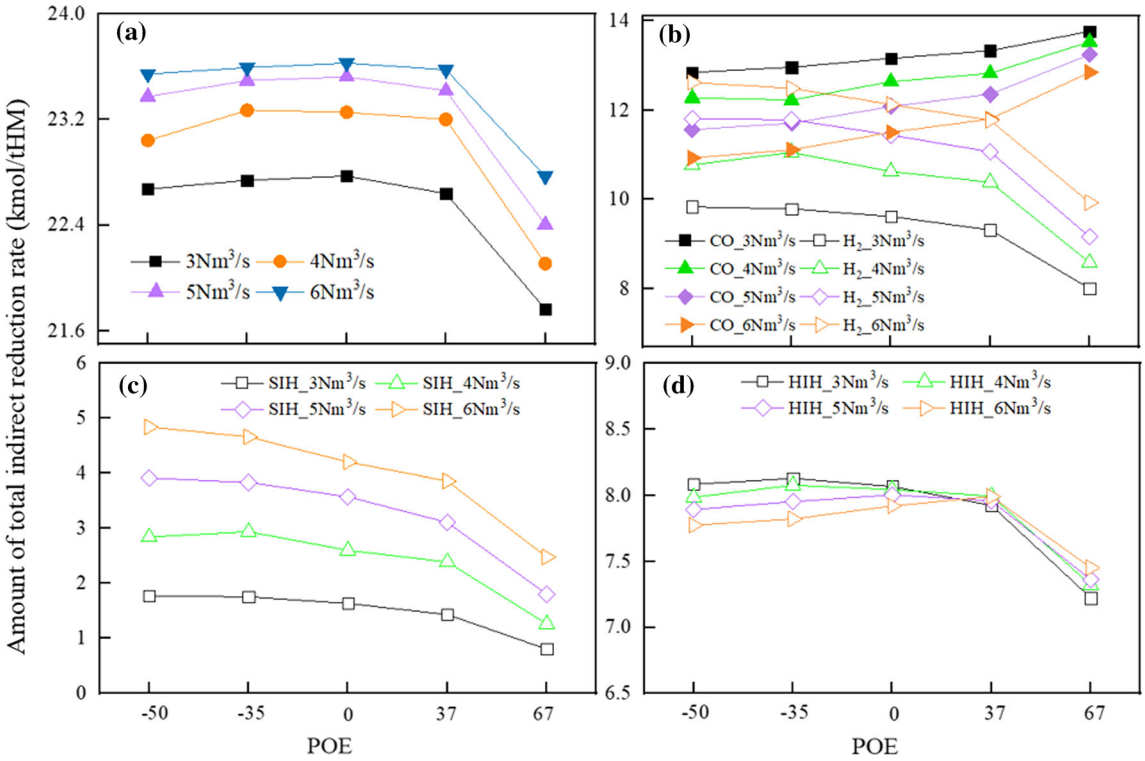

Fig. 13—Indirect reduction rates as a function of POE for different gas components: (*a*) total gas, (*b*) CO and H_2, (*c*) SIH, and (*d*) HIH at different SIH flow rates.

significant and then becomes gradual with increasing SIH flow rate. In contrast, the CO and H_2 indirect reduction rates change linearly with the SIH flow rate for a given POE (Figure 13(b)). When the SIH flow rate becomes larger, the CO indirect reduction rate decreases and its curve with respect to POE shifts down. At the same time, the H_2 indirect reduction rate increases, and its curve shifts up. Consequently, the difference between the two reduction rates becomes smaller at a larger POE. These minorly opposite results at relatively large POE values lead to nearly the same total indirect reduction rate.

The H_2 indirect reduction reaction is further analyzed to examine the difference between the contributions by the SIH and HIH, as shown in Figures 13(c) and (d), respectively. It shows that the H_2 indirect reduction rate change is mainly caused by the hydrogen injected into the furnace through shaft tuyeres. Overall, the SIH indirect reduction rate increases as the SIH flow rate increases for a given POE, which is attributed to the intensified hydrogen atmosphere. Conversely, the HIH indirect reduction rate varies with the SIH flow rate only within relatively small ranges. It decreases at relatively small POEs but increases at relatively large POEs. This decrease should be because of the shrunken dry zone resulting from the CZ elevation at a higher SIH flow rate, which reduces the space for H_2 indirect reduction. Differently, the increase in the HIH indirect reduction rate at relatively large POEs is attributed to the increased dry zone temperature.

V. CONCLUSIONS

The effects of top burden distribution in terms of peripheral opening extent (POE) on the flow and thermochemical behaviors and overall performance of the hydrogen BF are studied by a recently developed CFD process model. The BF is operated with hydrogen injection through both shaft and hearth tuyeres. The cases of loading more ore (negative POE values) or more coke (positive POE values) near the furnace wall are considered with constant coke rate and bosh gas volume and temperature. Different flow rates of shaft-injected hydrogen (SIH) are also considered. The major findings are summarized as follows:

- As the POE increases from − 50 to 67 for a given SIH flow rate, the flow of SIH is better developed with larger velocity magnitudes. This flow is generally confined within the peripheral region and increases heat loss through the furnace wall. This increased heat loss and the reduced bed permeability resulting from the re-distribution of some ore particles in the peripheral region into other radial locations cause an enlarged low-temperature zone in the upper part of BF. The low-temperature region and the less contact between iron ore and SIH decrease the H_2 indirect reduction rates. The result is opposite to the CO indirect reduction rate that increases with the increase of POE because of the enlarged reaction zone resulting from the lowered CZ. With the above transport phenomena, the HM temperature increases first to a

maximum and then drops drastically with increasing POE, which is opposite to the productivity trend. An optimum peripheral opening extent is thus identified with the maximum HM temperature corresponding to the biggest coke saving, relatively low pressure drop, and good H_2 and CO utilization efficiency. The optimum burden distribution has uniform coke and ore layer thicknesses near the furnace wall under the condition considered.

- Increasing the SIH flow rate improves the shaft injection penetration into the bed column, which is not as significant as that achieved by increasing POE. It also helps to overcome the low temperature caused by a higher POE, enhancing the SIH indirect reduction rate. Competing with the intensified SIH indirect reduction rate, the CO indirect reduction rate drops at a higher SIH flow rate. In contrast, the indirect reduction by hearth-injected hydrogen is generally less affected. It is enhanced by a higher SIH flow rate at relatively small POEs but reverses at relatively large POEs. Due to opposite trends of CO and H_2 indirect reduction rates with respect to SIH flow rate, the phenomenon that the HM temperature increases with POE first to a maximum and then drops drastically becomes less apparent at relatively high SIH flow rates. The increase becomes almost trivial when the POE is relatively small, and the SIH flow rate is relatively large.

ACKNOWLEDGMENTS

The authors are grateful to the Australian Research Council (ARC) and the Natural Science Foundation of China (NSFC) (5203000616) for the financial support of this work, the National Computational Infrastructure (NCI) for the use of high-performance computational facilities, and CAFFA3D for making a useful code available for free use and adaptation.

FUNDING

Open Access funding enabled and organized by CAUL and its Member Institutions.

COMPETING INTERESTS

On behalf of all authors, the corresponding author states that there is no conflict of interest.

OPEN ACCESS

REFERENCES

1. C. Xu and D. Cang: *J. Iron Steel Res. Int.*, 2010, vol. 17, pp. 1–7.
2. X. Zhang, K. Jiao, J. Zhang, and Z. Guo: *J. Clean. Prod.*, 2021, vol. 306, p. 127259.
3. K. Ma, J. Deng, G. Wang, Q. Zhou, and J. Xu: *Int. J. Hydrog.*, 2021, vol. 46, pp. 26646–64.
4. W. Liu, H. Zuo, J. Wang, Q. Xue, B. Ren, and F. Yang: *Int. J. Hydrog.*, 2021, vol. 46, pp. 10548–69.
5. Y. Chen and H. Zuo: *Ironmak. Steelmak.*, 2021, vol. 48, pp. 749–68.
6. J. Tang, M. Chu, F. Li, C. Feng, Z. Liu, and Y. Zhou: *Int. J. Miner. Metall.*, 2020, vol. 27, pp. 713–23.
7. J. Zhao, H. Zuo, Y. Wang, J. Wang, and Q. Xue: *Ironmak. Steelmak.*, 2019, vol. 47, pp. 296–306.
8. J. Li, S. Kuang, L. Jiao, L. Liu, R. Zou, and A. Yu: *Fuel*, 2022, vol. 323, p. 124368.
9. Baowu: The project guideline and declaration notice of china baowu low-carbon metallurgy innovation fund 2021, http://www.baowugroup.com/glcmia/detail/221899.
10. M. Ichida, K. Nishihara, K. Tamura, M. Sugata, and H. Ono: *ISIJ Int.*, 1991, vol. 77, pp. 1617–24.
11. Z. Li, S. Kuang, S. Liu, J. Gan, A. Yu, Y. Li, and X. Mao: *Powder Technol*, 2019, vol. 353, pp. 385–97.
12. M. Nikus, H. Saxen, and A. Bulsari: Iron & Steel Soc Aime, Warrendale,1996.
13. H. Saxén, M. Nikus, and J. Hinnelä: *Steel Res. Int.*, 1998, vol. 69, pp. 406–12.
14. J. Wei, X. Chen, J. Kelly, and Y. Cui: *Ironmak. Steelmak.*, 2015, vol. 42, pp. 533–41.
15. F. Zhenwei, Y. Li, Z. Zhang, G. Qiang, and Z. Zhao: *Iron Mak.*, 2000, vol. 19, pp. 1–4.
16. J. Chen, H. Zuo, Q. Xue, and J. Wang: *Powder Technol.*, 2022, vol. 398, p. 117055.
17. S.B. Kuang, Z.Y. Li, D.L. Yan, Y.H. Qi, and A.B. Yu: *Miner. Eng.*, 2014, vol. 63, pp. 45–56.
18. X. Yu and Y. Shen: *Metall. Mater. Trans. B*, 2020, vol. 51B, pp. 2079–94.
19. S. Liu, Z. Zhou, K. Dong, A. Yu, D. Pinson, and J. Tsalapatis: *Steel Res. Int.*, 2015, vol. 86, pp. 651–61.
20. C. Ho, S. Wu, H. Zhu, A. Yu, and S. Tsai: *Miner. Eng.*, 2009, vol. 22, pp. 986–94.
21. T. Mitra and H. Saxén: *Comput. Part. Mech.*, 2016, vol. 3, pp. 541–55.
22. Z. Dong, Q. Xue, H. Zuo, X. She, J. Li, and J. Wang: *ISIJ Int.*, 2016, vol. 56, pp. 1588–97.
23. X. Dong, A. Yu, J. Yagi, and P. Zulli: *ISIJ Int.*, 2007, vol. 47, pp. 1553–70.
24. S. Kuang, Z. Li, and A. Yu: *Steel Res. Int.*, 2018, vol. 89, p. 1700071.
25. J. Yagi: *ISIJ Int.*, 1993, vol. 33, pp. 619–39.
26. H. Nogami, Y. Kashiwaya, and D. Yamada: *ISIJ Int.*, 2012, vol. 52, pp. 1523–27.
27. J. Tang, M. Chu, F. Li, C. Feng, Z. Liu, and Y. Zhou: *J. Miner. Metall.*, 2020, vol. 27, pp. 713–23.
28. M. Chu, H. Nogami, and J. Yagi: *ISIJ Int.*, 2004, vol. 44, pp. 801–08.
29. Z. Li, S. Kuang, A. Yu, J. Gao, Y. Qi, D. Yan, Y. Li, and X. Mao: *Metall. Mater. Trans. B*, 2018, vol. 49B, pp. 1995–2010.

30. L. Jiao, S. Kuang, A. Yu, Y. Li, X. Mao, and H. Xu: *Metall. Mater. Trans. B*, 2019, vol. 51B, pp. 258–75.
31. L. Jiao, S. Kuang, L. Liu, A. Yu, Y. Li, X. Mao, and H. Xu: *Metall. Mater. Trans. B*, 2020, vol. 52B, pp. 138–55.
32. L. Jiao, S. Kuang, Y. Li, X. Mao, H. Xu, and A. Yu: *Metall. Mater. Trans. B*, 2021, vol. 52B, pp. 2642–58.
33. A. Pr, H. Nogami, and J. Yagi: *ISIJ Int*., 1997, vol. 37, pp. 748–55.
34. K. Yang, S. Choi, J. Chung, and J. Yagi: *ISIJ Int*., 2010, vol. 50, pp. 972–80.
35. X.F. Dong, A.B. Yu, S.J. Chew, and P. Zulli: *Metall. Mater. Trans. B*, 2010, vol. 41B, pp. 330–49.
36. G.X. Wang, S.J. Chew, A.B. Yu, and P. Zulli: *Metall. Mater. Trans. B*, 1997, vol. 28B, pp. 333–43.
37. S.J. Zhang, A.B. Yu, P. Zulli, B. Wright, and U. Tüzün: *ISIJ Int*., 1998, vol. 38, pp. 1311–19.
38. H. Nie, Z. Li, S. Kuang, L. Yan, W. Zhong, A. Yu, X. Mao, and H. Xu: *Fuel*, 2021, vol. 296, p. 120662.
39. L. Liu, B. Guo, S. Kuang, and A. Yu: *Metall. Mater. Trans. B*, 2020, vol. 51B, pp. 2211–29.
40. L. Liu, S. Kuang, L. Jiao, B. Guo, and A. Yu: *Fuel*, 2022, vol. 315, p. 122832.
41. G. Usera, A. Vernet, and J. Ferré: *Flow Turbul. Combust*., 2008, vol. 81, pp. 471–95.
42. H.Q. Nie, A.B. Yu, L.L. Jiao, X.M. Mao, H.F. Xu, and S.B. Kuang: *Metall. Mater. Trans. B*, 2022, vol. 53B, pp. 2712–34.